Energy Materials

Supplementary Materials

Design of quasi-solid-state electrolyte with continuous Li^+ pathways via bridging cellulose and α-Li_2TiO_3 for lithium batteries

Dongxue Chu[1,2], Rui Gao[3,*], Linglong Hu[1], Hongji Xu[1], Daming Yang[1], Zhongjun Chen[4], Ze Gao[1], Wanxia Huang[4], Ming Feng[1,5,*]

[1]Key Laboratory of Functional Materials Physics and Chemistry of the Ministry of Education, Jilin Normal University, Changchun 130103, Jilin, China.

[2]College of Chemistry, Jilin Normal University, Siping 136000, Jilin, China.

[3]Institute for Clean Energy Technology, North China Electric Power University, Beijing 102206, China.

[4]Beijing Synchrotron Radiation Facility, Institute of High Energy Physics, Chinese Academy of Sciences, Beijing 100049, China.

[5]Changbaishan Laboratory, Jilin University, Changchun 130012, Jilin, China.

[*]**Corresponding to:** Prof. Ming Feng, Key Laboratory of Functional Materials Physics and Chemistry of the Ministry of Education, Jilin Normal University, Changchun 130103, Jilin, China. E-mail: mingfeng@jlnu.edu.cn; Dr. Rui Gao, Institute for Clean Energy Technology, North China Electric Power University, Beijing 102206, China. E-mail: r55gao@ncepu.edu.cn

Pouch Cell Assembly

The pouch cell was fabricated by sandwiching a BC/ZIF-67@Li_2TiO_3 QSSE between an NCM811 cathode (areal loading: 10 mg cm^{-2}, dimensions: 5 cm × 3 cm) and a 50 μm lithium foil anode (areal capacity: 9.65 mAh cm^{-2}; dimensions: 5.2 cm × 3.2 cm). All assembly steps were conducted in a glovebox filled with high-purity argon (H_2O < 0.1 ppm, O_2 < 0.1 ppm), and the resulting N/P ratio was calculated to be 4.8.

Electrochemical characterization

According to previously reported literature [S1]: The Li^+ conductivity of electrolytes within the separators was evaluated via Electrochemical Impedance Spectroscopy (EIS) in a frequency range from 1×10^6 to 1 Hz to obtain the electrolyte resistance (R_s). A solid electrolyte with a specific thickness was sandwiched between two stainless steel plates. The Li^+ conductivity (σ) was calculated by Eq:

$$\sigma = L/R_s \times S \quad (1)$$

where L is certain thickness, S is surface area. The activation energy (Ea) could be by fitting Li^+ conductivity as a function of temperature (T).

The activation energy calculation method is based on the Arrhenius fundamental equation [S2,S3]:

$$\sigma = \sigma_0 \exp\left(\frac{-E_a}{k_B T}\right) \quad (2)$$

σ_0 is pre-exponential factor, E_a is activation energy, k_B is Boltzmann constant =8.617×10^{-5} eV·K^{-1}, T is absolute temperature (K).

The Li^+ transference number (t_{Li^+}) was determined using alternating-current (AC) impedance and direct-current (DC) potentiostatic polarization measurements on Li/Li symmetric battery. t_{Li^+} was calculated based on the Eq:

$$t_{Li^+} = \frac{I_{ss}(V - I_0 R_{int}{}^0)}{I_0(V - I_{ss} R_{int}{}^{ss})} \quad (3)$$

Where V = 20 mV. Initial AC impedance measurements were performed on fresh cells to obtain the initial interfacial resistance ($R_{int}{}^0$), corresponding to the semicircle

diameter in the high-to-medium frequency region. Subsequently, the initial current (I_0) and steady-state current (I_{ss}) were recorded during DC potentiostatic polarization at a constant potential of 20 mV for 1000 s. R_{int}^{ss} denotes the interfacial resistance after DC polarization.

Li-ion full cells were assembled by using $LiNi_{0.8}Mn_{0.1}Co_{0.1}O_2$ (NCM) or $LiFePO_4$ (LFP) as cathode, lithium metal as anode. Commercial NCM or LFP powders mixed with super P and PVDF (mass ratio 8:1:1) were coated on 15 um carbon coated Al foil. Before battery assembling, cellulose-based separators were soaked in to electrolyte for 12 h and then surface dried with filter paper. During battery assembling, additional 15 µl electrolyte were add. The full-cell battery was first activated by cycling at a low current for several cycles, followed by evaluating its cycling performance at a high current. All cell tests were conducted at 25 ℃, the voltage window for rate tests and the corresponding rate profiles of Li//NCM cells were set to 2.8 - 4.5 V, while the cycling tests and their associated capacity–voltage curves at various cycles adopted a voltage range of 2.8 - 4.3 V.

Model formulation:

1. Phase-Field Model

The evolution of the phase-field variable, ξ, which distinguishes the electrode ($\xi = 1$) from the electrolyte ($\xi = 0$), is governed by the Allen-Cahn equation [S4].

$$\frac{\partial \xi}{\partial t} = -L_\sigma \left(\frac{\delta f_{loc}}{\delta \xi} - \kappa_\xi \nabla^2 \xi \right) - L_\eta \frac{\delta f_{el}}{\delta \xi} h'(\xi)$$

- ξ: Phase-field variable.
- t: Time.
- L_σ: Interfacial mobility related to surface energy.
- f_{loc}: Local free energy density (double-well potential).
- κ_ξ: Gradient energy coefficient for the interface.
- L_η: Electrochemical mobility related to reaction kinetics.

- f_{el}: Electrochemical free energy density.
- $h(\xi)$: Interpolation function (e.g., $h(\xi) = \xi^3(6\xi^2 - 15\xi + 10)$).

2. Lithium Ion Transport (Concentration Field)

The transport of Li^+ in the electrolyte is governed by the Nernst-Planck equation, including diffusion and migration [S5].

$$\frac{\partial c}{\partial t} = \nabla \cdot \left(D_{eff}(\xi)\nabla c + \frac{D_{eff}(\xi)cF}{RT}\nabla\phi_l \right) + \frac{j_{loc}t_+}{F} \mid \nabla\xi \mid$$

- c: Concentration of Li^+ in the electrolyte.
- $D_{eff}(\xi)$: Effective diffusivity, interpolated between electrolyte and electrode.
- F: Faraday's constant.
- R: Universal gas constant.
- T: Absolute temperature.
- ϕ_l: Electric potential in the liquid electrolyte.
- j_{loc}: Local current density (from Butler-Volmer equation).
- t_+: Transference number of Li^+.

3. Electric Field (Charge Conservation)

The electrostatic potentials in the solid electrode (ϕ_s) and the liquid electrolyte (ϕ_l) are solved [S5].

In the Electrode:

$$\nabla \cdot (\sigma_s(\xi)\nabla\phi_s) = j_{loc} \mid \nabla\xi \mid$$

In the Electrolyte:

$$\nabla \cdot \left(\kappa_{eff}(\xi)\nabla\phi_l + \frac{2\kappa_{eff}(\xi)RT}{F}(1 - t_+)\nabla \ln\, c \right) = -j_{loc} \mid \nabla\xi \mid$$

- ϕ_s: Electric potential in the solid electrode.
- $\sigma_s(\xi)$: Electrical conductivity of the solid phase.
- $\kappa_{eff}(\xi)$: Effective ionic conductivity of the electrolyte.
- j_{loc}: Local current density.

Supplementary Table 1. The key parameters and computational settings

Parameters	Values
sigmaE (solution conductivity)	0.1 [S/m]
sigmaS (dendrite conductivity)	1×10^{7} [S/m]
D_E (ion diffusion coefficient)	0.2×10^{-14} [m^2/s]
L_sigma (Interfacial mobility)	1×10^{-6} [m^3/(J×s)]

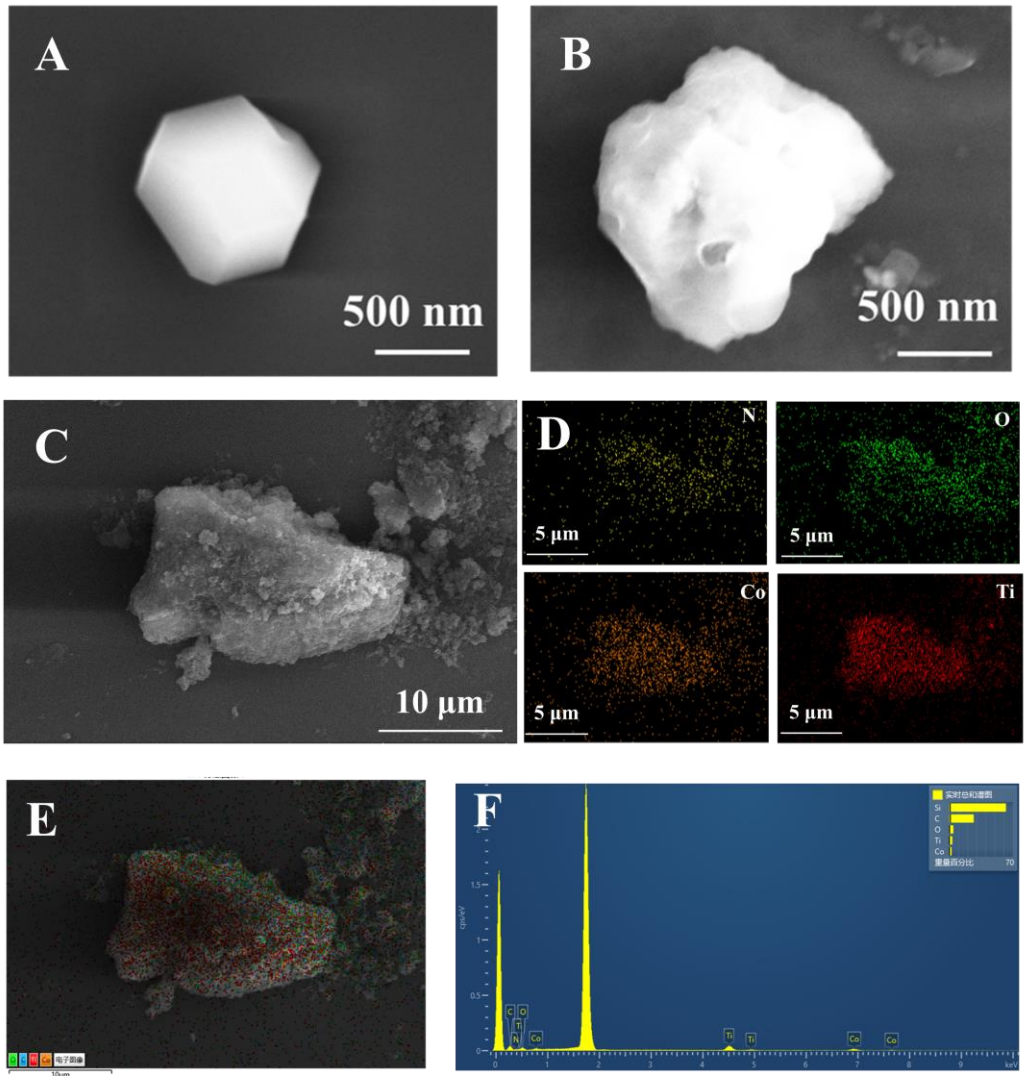

Supplementary Figure 1. SEM images of ZIF-67 (A), (B-C) ZIF-67@Li_2TiO_3 powder and EDS mapping (D-F).

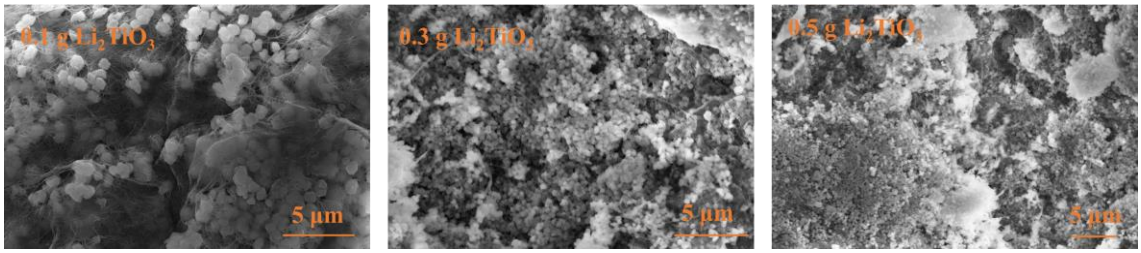

Supplementary Figure 2. SEM images of BC/ZIF-67@Li_2TiO_3 membranes with different Li_2TiO_3 addition amounts.

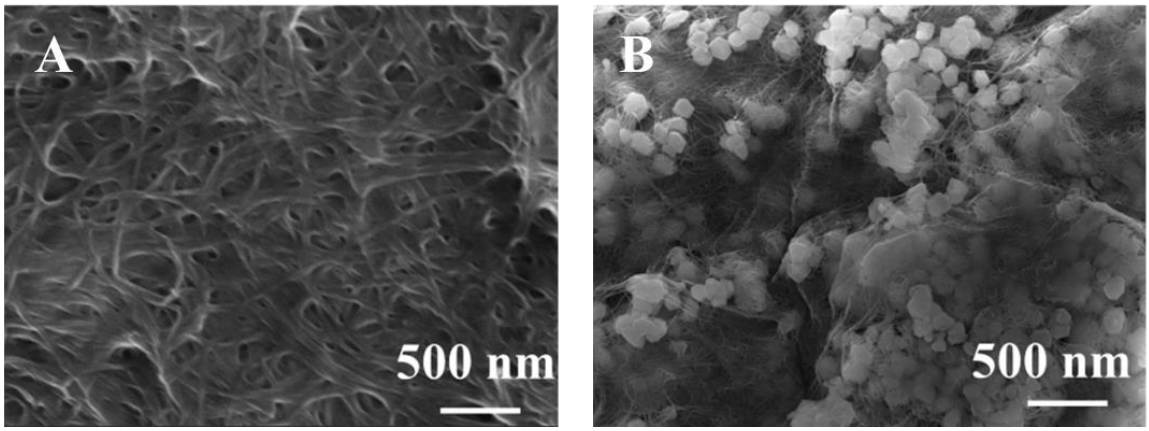

Supplementary Figure 3. SEM images of BC (A) and BC/ZIF-67 (B) membranes.

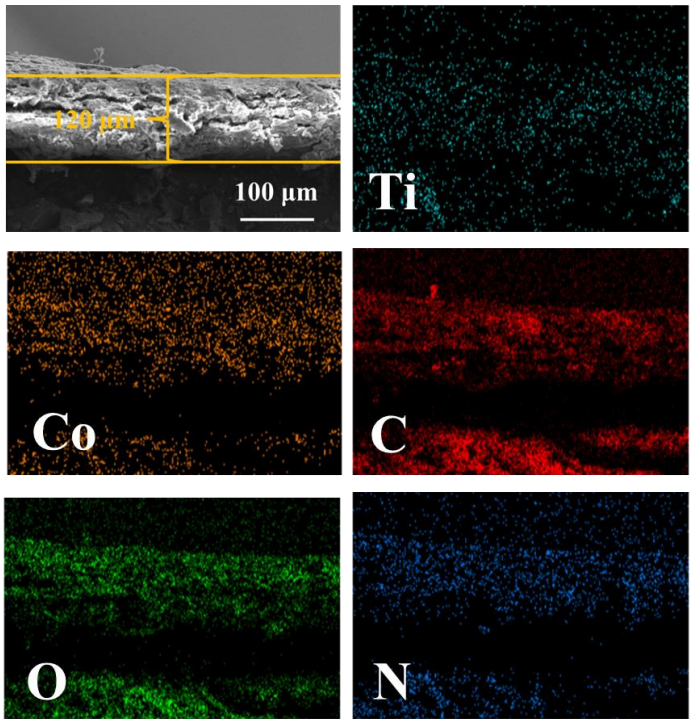

Supplementary Figure 4. The SEM images of BC/ZIF-67@Li_2TiO_3 membrane cross-sectional view and EDS mapping.

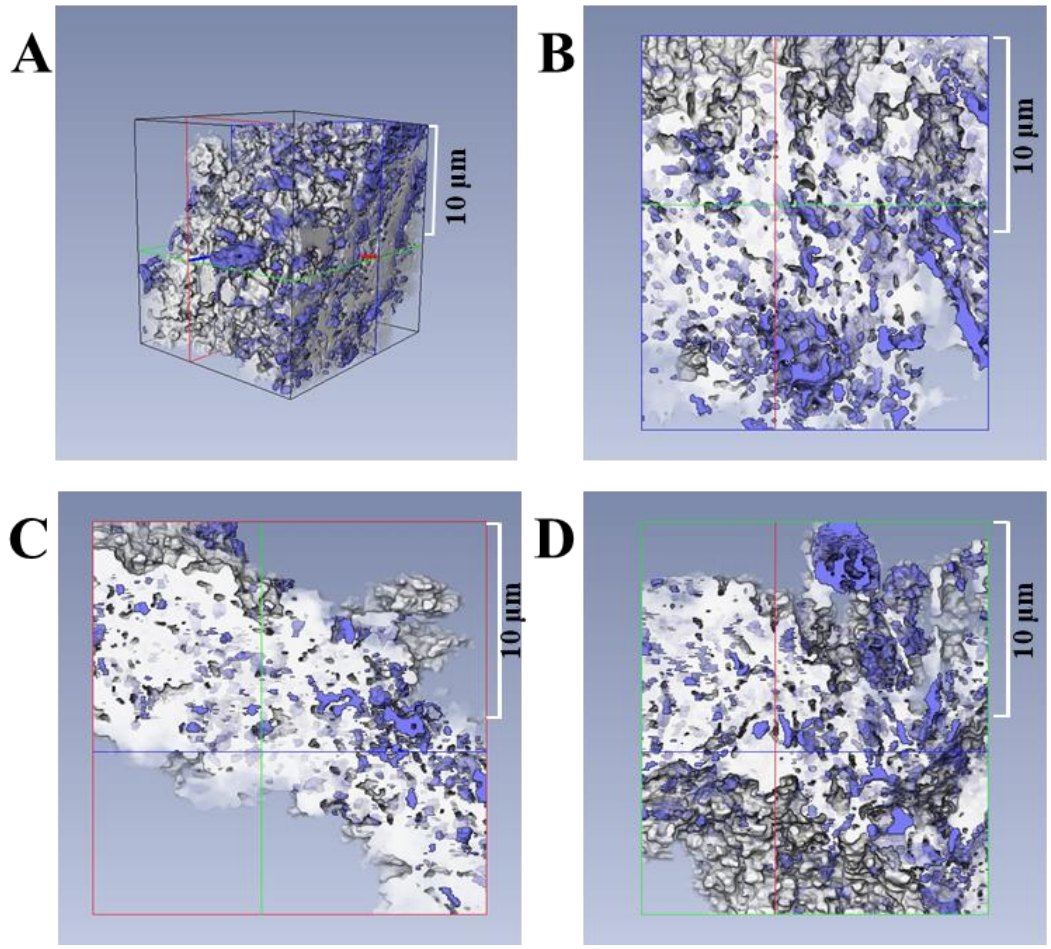

Supplementary Figure 5. BC/ZIF-67@Li_2TiO_3 CT images of the diaphragm at different angles.

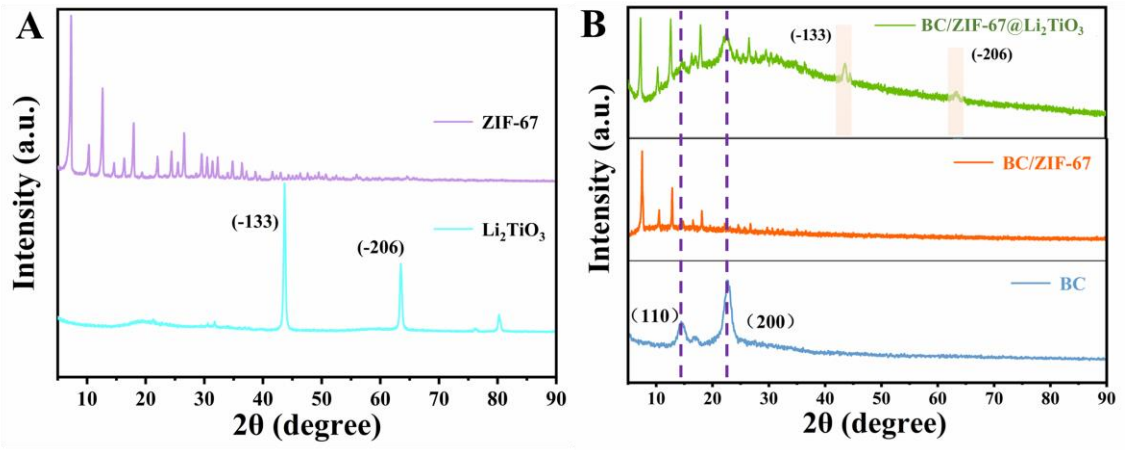

Supplementary Figure 6. The XRD patterns of (A) raw powder, (B) BC BC/ZIF-67 and BC/ZIF-67@Li_2TiO_3 membranes.

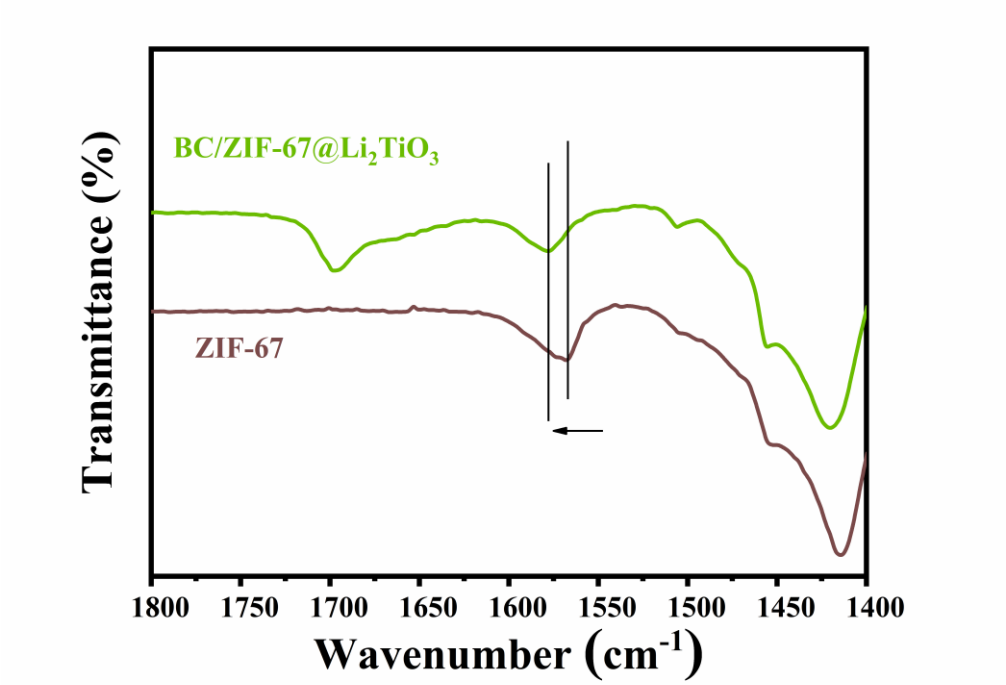

Supplementary Figure 7. The FT-IR patterns of ZIF-67 powder, and BC/ZIF-67@Li_2TiO_3 membrane.

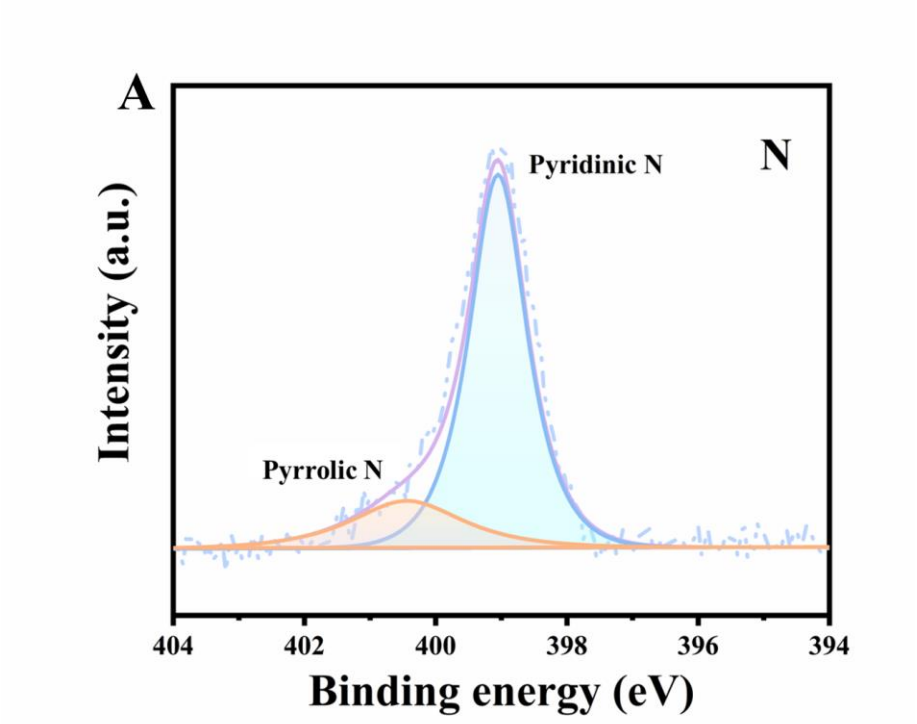

Supplementary Figure 8. The XPS spectrum of N, O in the BC/ZIF-67@Li_2TiO_3 membrane.

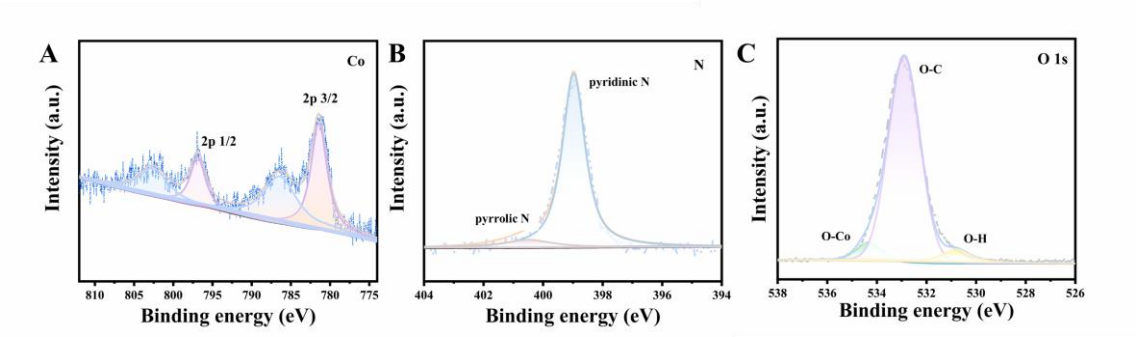

Supplementary Figure 9. The XPS spectrum of Co (A), N (B), O (C) in the BC/ZIF-67 membrane.

Supplementary Figure 10. Precursor solution contact angle of BC/ZIF-67 membrane at 1s.

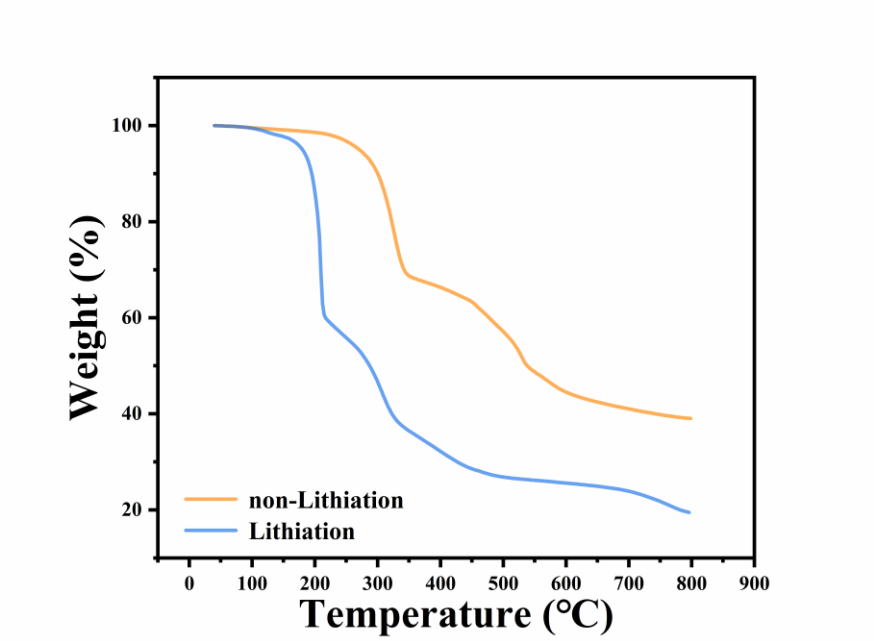

Supplementary Figure 11. Thermogravimetric curves of BC/ZIF-67@Li_2TiO_3 membrane before and after lithiation.

As shown in Supplementary Figure 11. there are two obvious mass loss at 200~340℃ and above 400℃ for BC/ZIF-67@Li_2TiO_3 membranes. The first at low temperature represent for the oxidation of BC and the second for ZIF-67 decomposition. In sharp contrast, the lithiated sample exhibits a different behavior with four distinct decomposition stages. The peak value of the first derivative directly identifies each reaction stage. For the lithiated sample, the weight loss below 120℃ is primarily attributed to the volatilization of the residual solvent. This mass loss is less than 1%, This result clearly proves that the liquid phase ratio in the system is below 1%. Next, the major weight loss around 170 °C is attributed to the decomposition of the lithium salt. The loss around 250 °C mainly represents the decomposition of the cellulose framework. Finally, the reaction stages above 400 °C are much more complex. This complexity is caused by the side reactions involving lithium salt decomposition products.

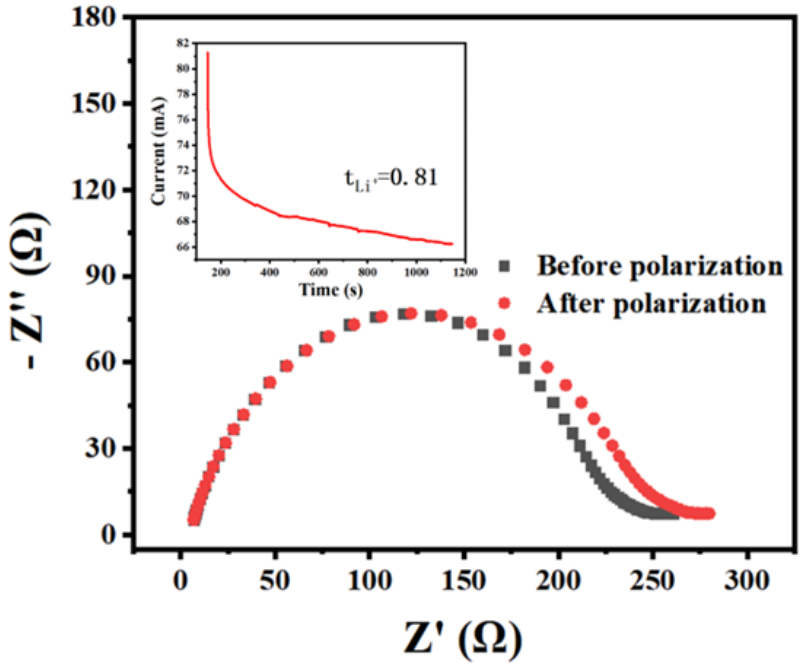

Supplementary Figure 12. EIS before and after polarization of the Li|BC/ZIF-67@Li_2TiO_3|Li LMB, the inset is current−time curve at 20 mV of polarization.

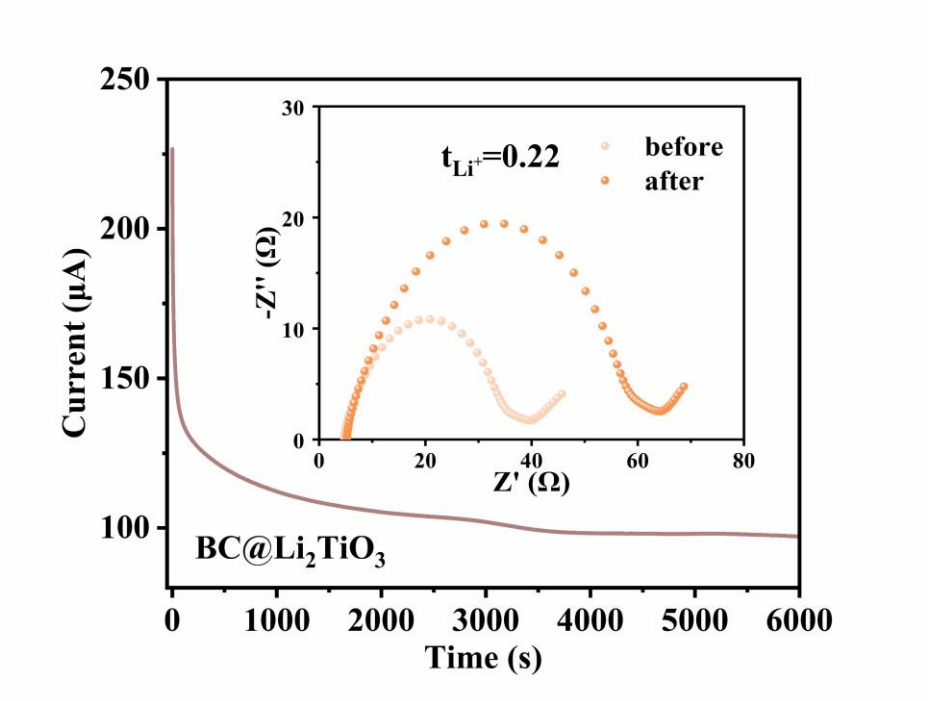

Supplementary Figure 13. EIS before and after polarization of the Li|BC/Li_2TiO_3|Li LMB, the inset is current−time curve at 20 mV of polarization.

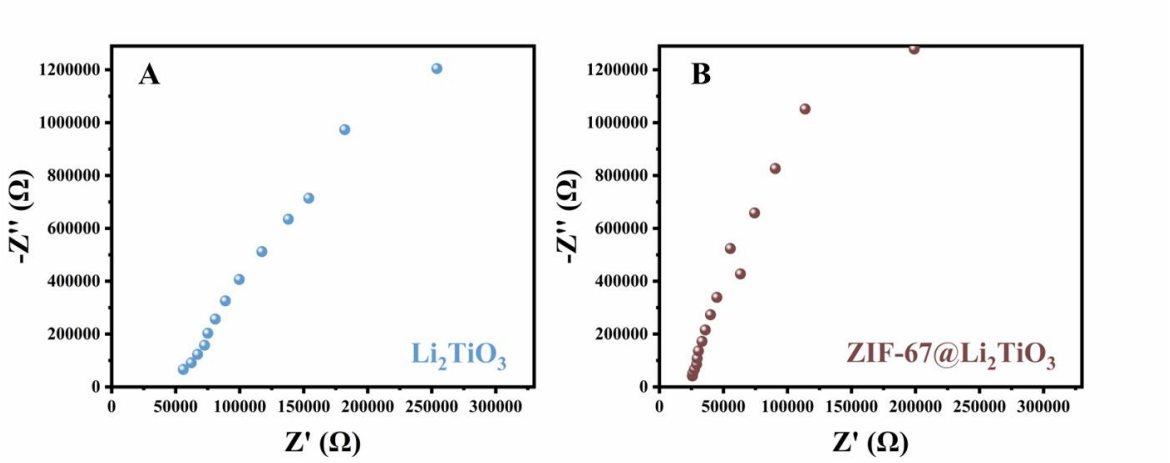

Supplementary Figure 14. EIS plots of α-Li_2TiO_3 (A), and ZIF-67@Li_2TiO_3 (B) pellet at 25℃.

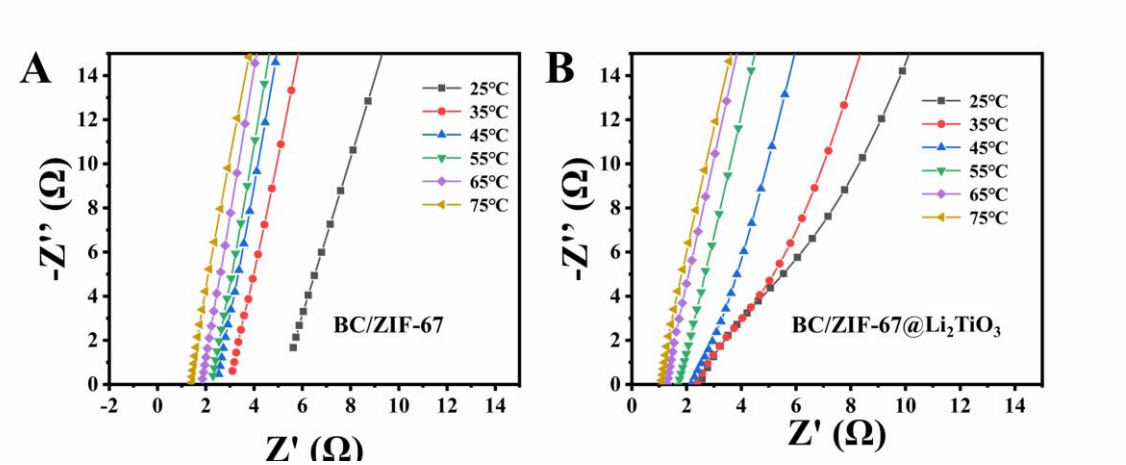

Supplementary Figure 15. EIS plots of BC/ZIF-67 (A) and BC/ZIF-67@ Li_2TiO_3 (B) QSSEs at different temperature.

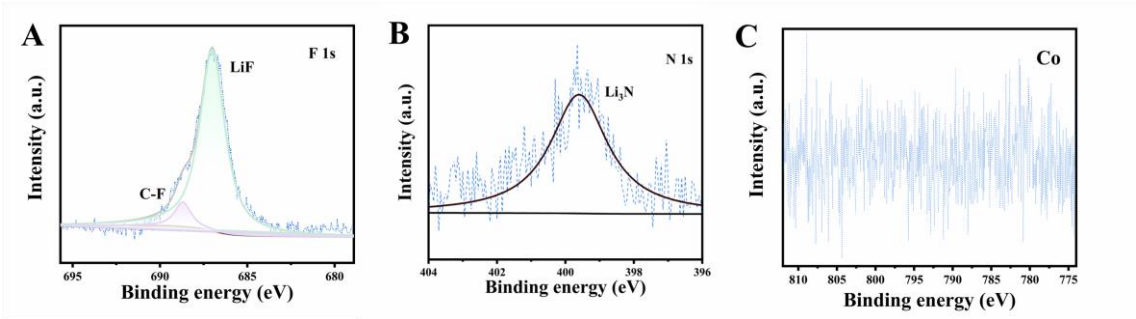

Supplementary Figure 16. F 1s, N 1s and Co 2p XPS spectra of Li metal anode from 800 h cycled Li|BC/ZIF-67@Li_2TiO_3|Li.

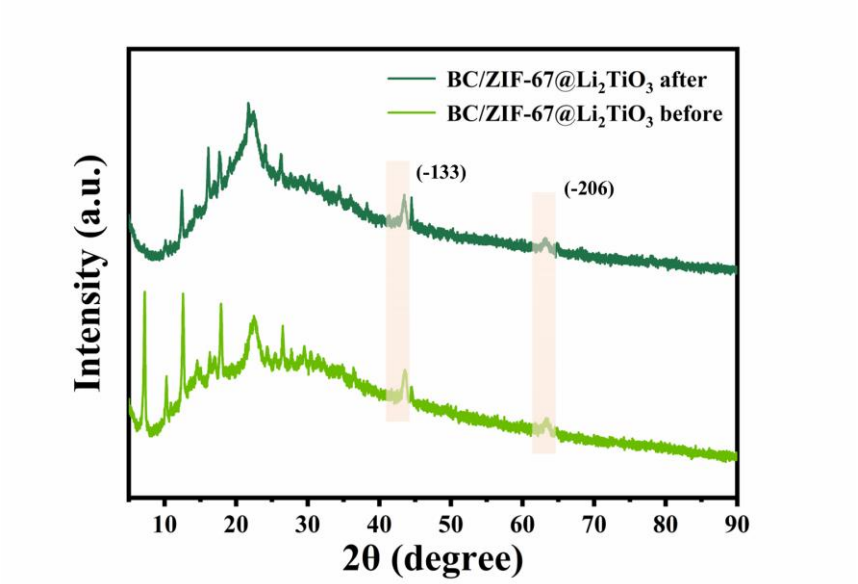

Supplementary Figure 17. The XRD pattern of BC/ZIF-67@Li_2TiO_3 QSSE after cycling.

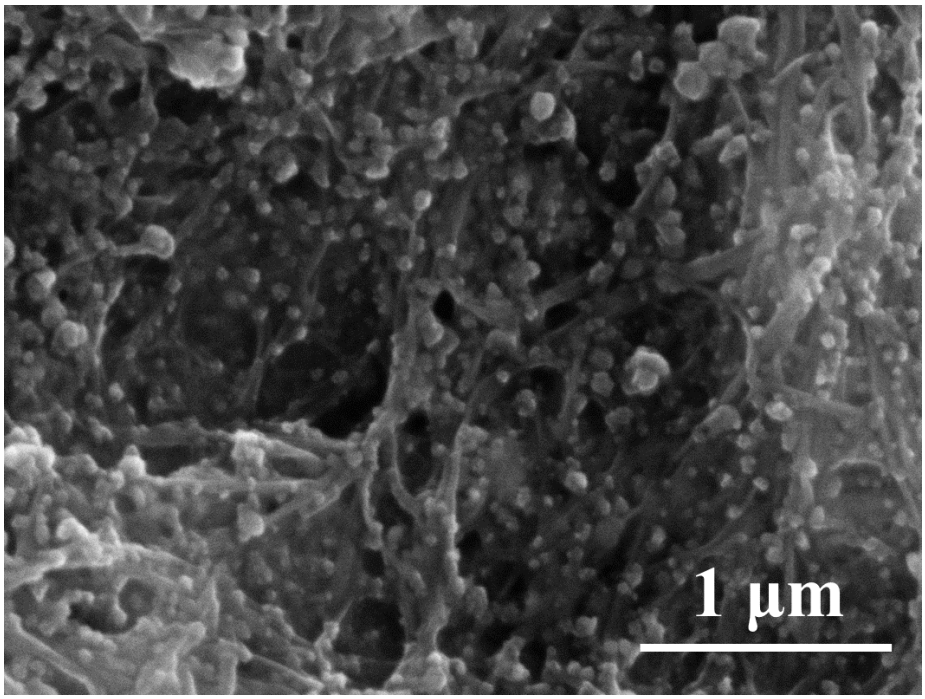

Supplementary Figure 18. SEM image of BC/ZIF-67@Li_2TiO_3 QSSE after 800 h cycle.

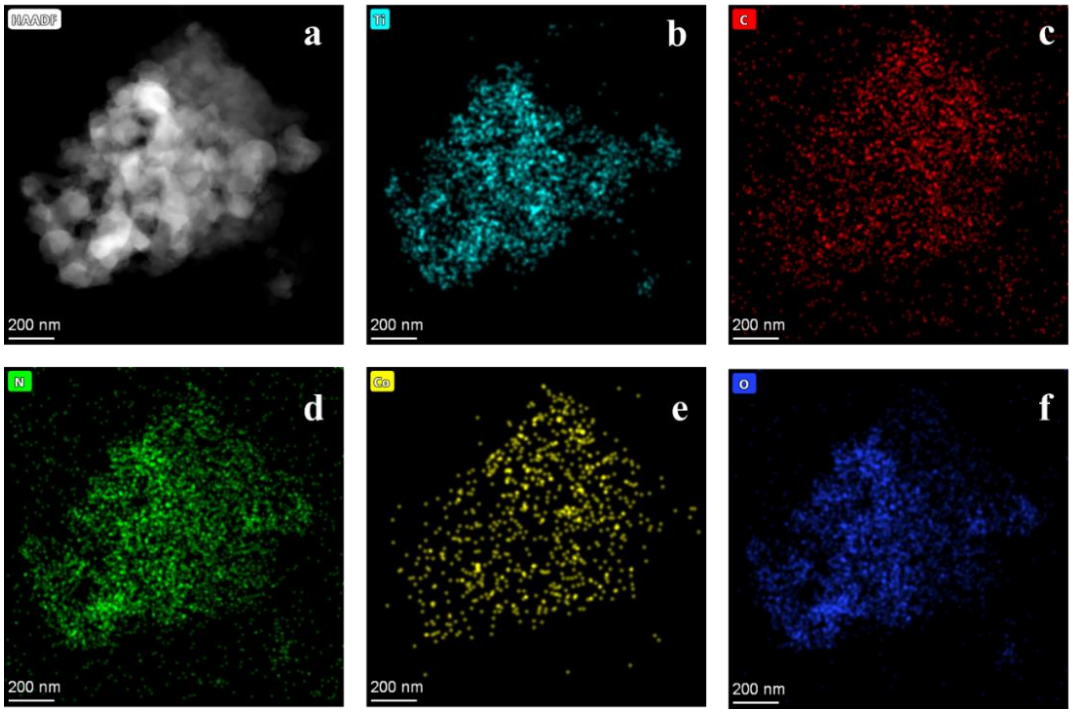

Supplementary Figure 19. (a) BC/ZIF-67@Li_2TiO_3 QSSE TEM images and (b-f) EDS mappings after 800 h cycles.

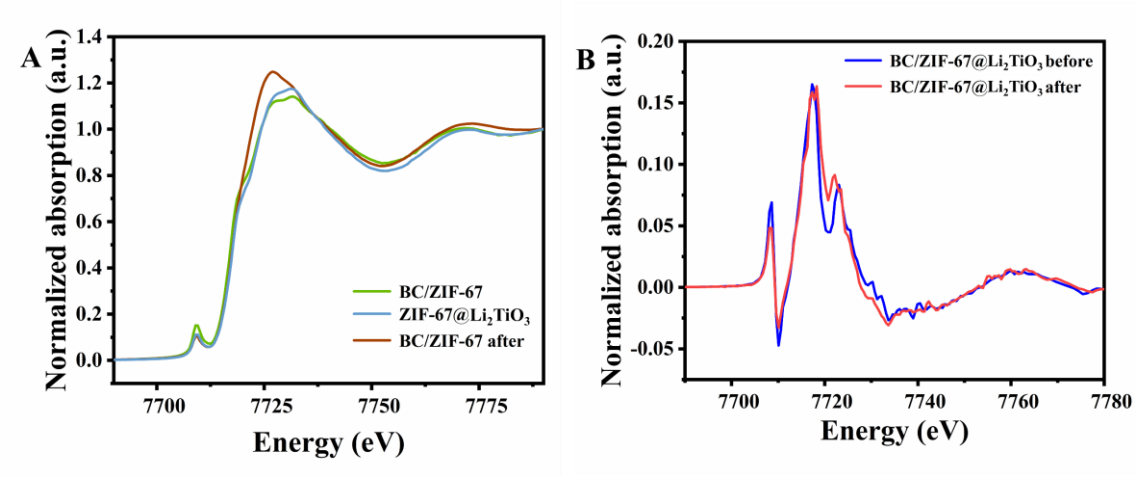

Supplementary Figure 20. (A) XANES for Co-K edge of BC/ZIF-67 membrane, ZIF-67@Li_2TiO_3 power, and after 200 h cycles BC/ZIF-67 QSSE. (B) The derivative plot of K-edge of Co for electrolyte film before and after cycling of BC/ZIF-67@Li_2TiO_3 QSSE.

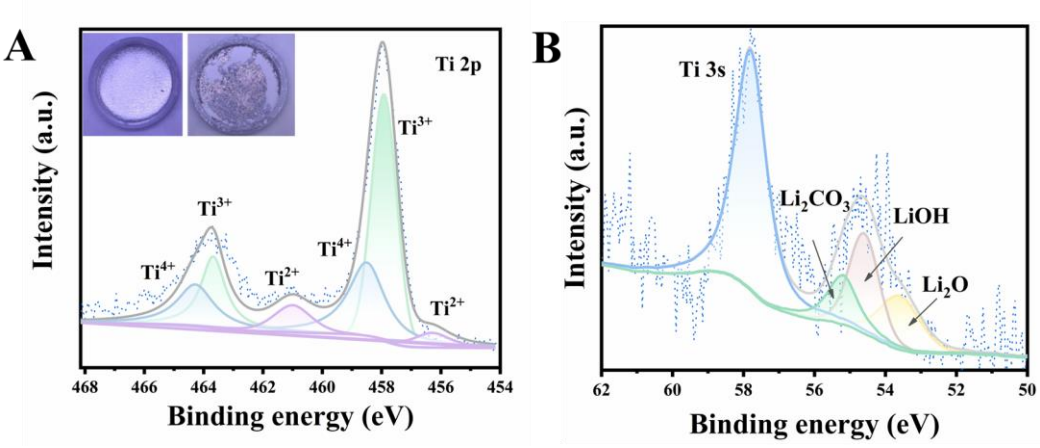

Supplementary Figure 21. (A) XPS spectra of Ti in the powder after the reaction between lithium metal and α-Li_2TiO_3 (the illustration is the surface morphology of lithium metal). (B) XPS spectra of Li in the powder after the reaction between lithium metal and α-Li_2TiO_3.

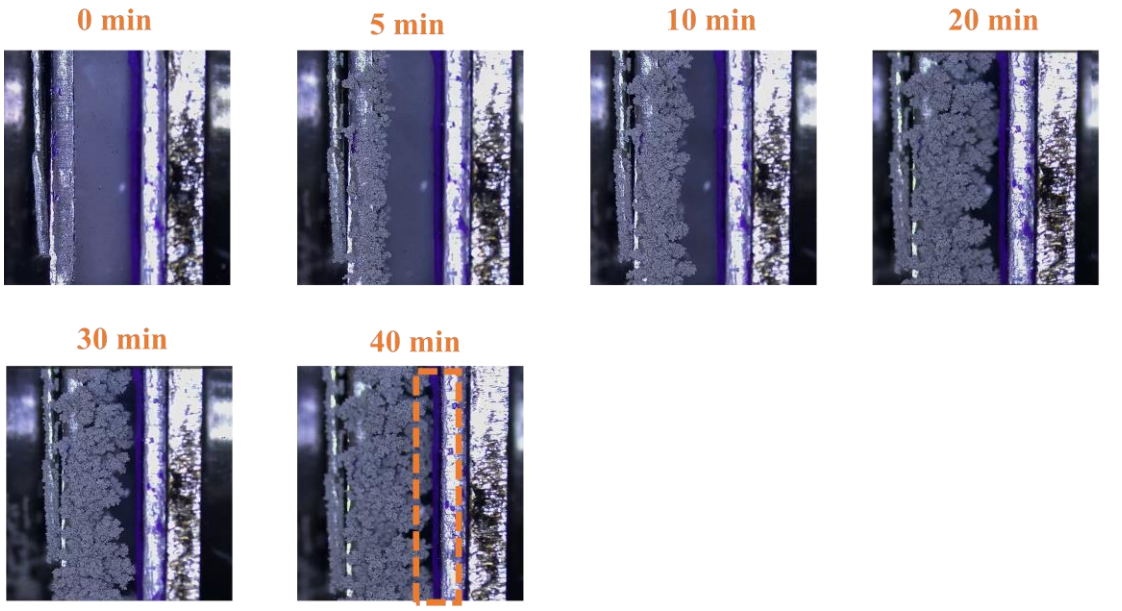

BC/ZIF-67

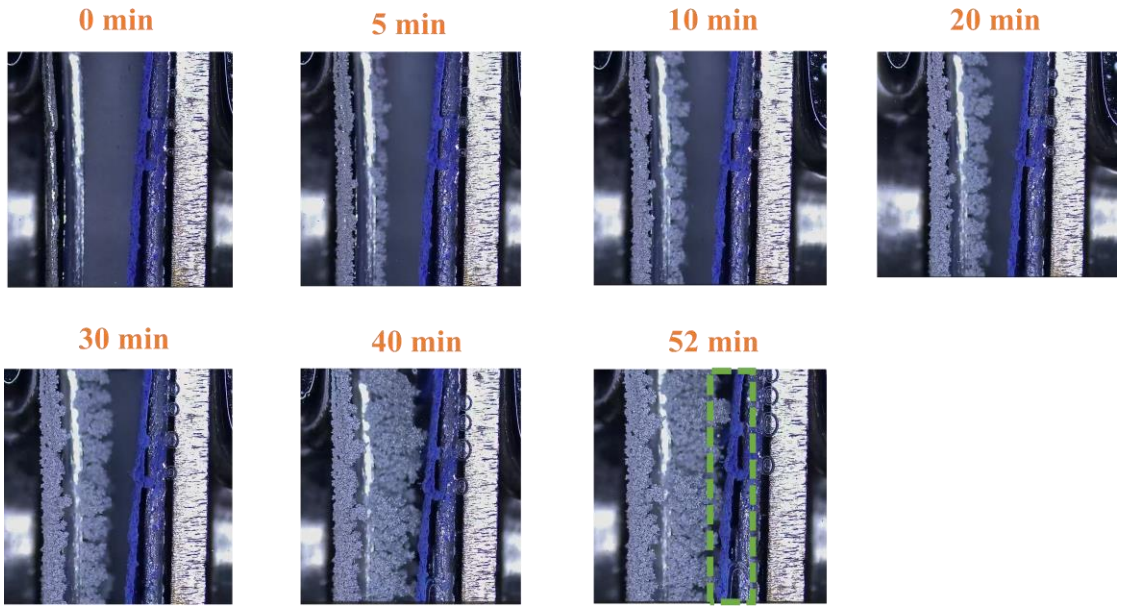

BC/ZIF-67@Li_2TiO_3

Supplementary Figure 22. In-situ optical microscopy images of BC/ZIF-67 and BC/ZIF-67@Li_2TiO_3 electrolyte interfaces at 10 mA for the duration of a single plating cycle.

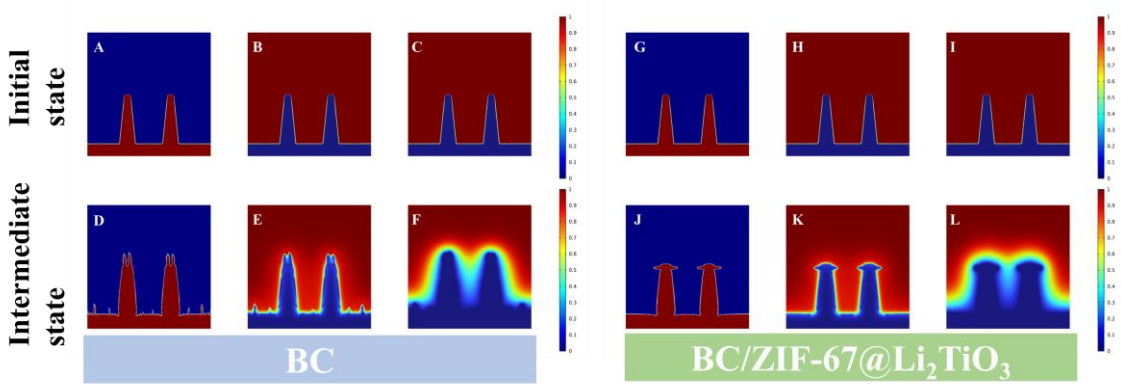

Supplementary Figure 23. The simulation initial state, and intermediate state results of lithium dendrite growth: (A-F) BC QSSE, (G-L) BC/ZIF-67@Li_2TiO_3 QSSE.

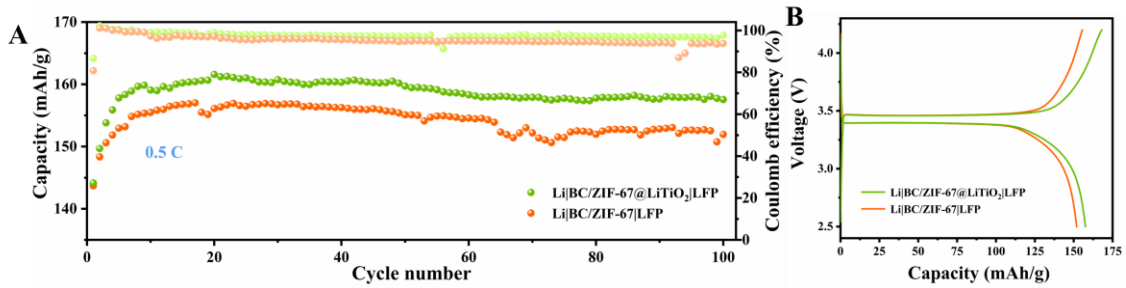

Supplementary Figure 24. (A) Cycling performance of Li|BC/ZIF-67@Li_2TiO_3|LFP and Li|BC/ZIF-67|LFP battery at 0.5 C. (B) the corresponding voltage profiles of Li|BC/ZIF-67@Li_2TiO_3|LFP and Li|BC/ZIF-67|LFP battery after 100 cycles at 0.5 C.

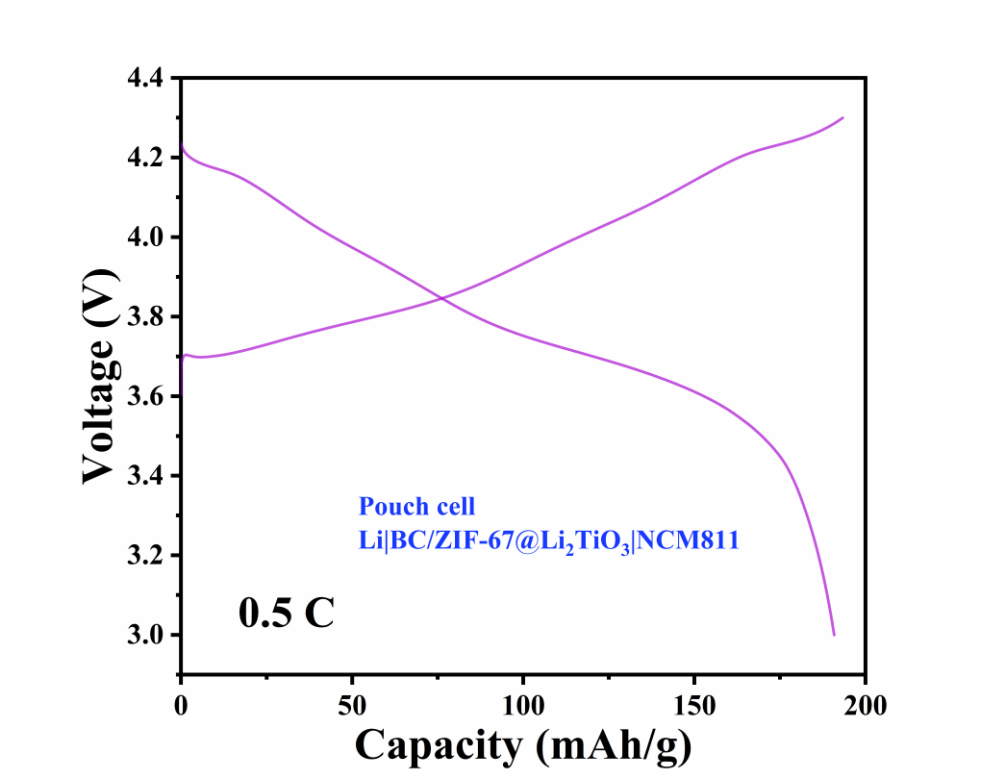

Supplementary Figure 25. Voltage profiles of Li|BC/ZIF-67@Li_2TiO_3|NCM811 pouch cell at 0.5 C with voltage window of 3.0 -4.3 V.

Supplementary Table 2. The comparison of full-cell parameters

	Cathode mass loading (mg cm^{-2})	**Li foil thickness (cm)**	**N/P ratio**	**electrolyte-to-capacity (mg/Ah)**
Li||LFP	2.5	0.06	272.47	149
Li||NCM811	5.7	0.06	101.57	54
Pouch cell Li||NCM811	10	0.005	4.8	22

Supplementary Table 3 Performance comparison of QSSEs

Materials	t_{Li^+}	σ (S/cm)	Electrochemical window (V)	full-cell Li//LFP	Ref
silica-cellulose-ether (SCE)	0.67	6.9×10^{-4}	4.87	200 cycles at 0.1 C	S6
PEGDA-CA/NMP/FEC	0.78	8.5×10^{-4}	-	-	S7
PVDF-CA/NATP	0.66	5.2×10^{-4}	5.0	-	S8
CA/PVDF/LiTFSI/ZIF-8(CPLZ)	0.57	6.9×10^{-4}	4.7	230 cycles at 0.5 C	S9
CLA-g-BN	0.79	1.25×10^{-3}	5.1	500 cycles at 0.5 C	S10
P(PEGDA)/CNF	-	1.93×10^{-3}	-	200 cycles at 0.1 C	S11
CTA-S-Al_2O_3	0.43	1.8×10^{-3}	5.2	530 cycles at 1C	S12
BC/ZIF-67@Li_2TiO_3	0.81	2.3×10^{-3}	5.41	900 cycles at 1C	This work

REFERENCES

[S1]Ge, D. H.; Peng, J.; Qu, G. L.; et al. Nanostructured Co(II)-based MOFs as promising anodes for advanced lithium storage. *New J. Chem.* **2016**, 40, 9238-9244.

[S2]Weng, S.; Zhang, X.; Yang, G.; et al. Temperature-dependent interphase formation and Li^+ transport in lithium metal batteries. *Nat. commun.* **2023**, 14 (1), 4474.

[S3]Zhao, Q.; Liu, X.; Zheng, J.; et al. Designing electrolytes with polymerlike glass-forming properties and fast ion transport at low temperatures. *P Natl. A Sci. India.* **2020**, 117 (42), 26053-26060.

[S4]Shen, X.; Zhang, R.; Shi, P.; Chen, X.; Zhang, Q. How does external pressure shape Li dendrites in Li metal batteries? *Adv. Energy Mater.* **2021**, 11, 2003416.

[S5]Di, L. B.; Huang, Z. J.; Gao, L.; et al. Dynamic control of lithium dendrite growth with sequential guiding and limiting in all- solid- state batteries. *Sci. Adv.* **2025**, 11, eadw9590.

[S6]Cao, W. Z.; Zhang, K.; Wang, J.; et al. Self-assembled silica-cellulose-ether ternary nanocomposite electrolytes for robust quasi-solid-state lithium metal batteries. *Energy storage material* **2025**, 75, 104067.

[S7]Wang, J. Q.; Huang X. Q.; Zhu, X. B.; et al. Tri-additive PEGDA-based quasi-solid electrolyte for enhanced ion transport and interface stability in Li-O_2 batteries. *Mater. Today Commun.* **2025**, 48, 113466.

[S8]Liu, Y. H.; Chen, P. X.; Kuo, Y. S.; et al. Solution-processed poly(vinylidene difluoride)-cellulose acetate/ $Na_{1+x}Al_xTi_{2-x}(PO_4)_3$ composite quasi-solid electrolyte for safe and high-performance quasi-solid-state sodium-ion batteries. *J Energy Storage* **2026,** 150, 120411.

[S9]Zhou, J.; Li, Y. W.; Zhu, Z. F.; et al. Regulation of Li-ion flux by metal organic framework in compact quasi-solid-state electrolyte for wide-temperature lithium-metal batteries. *Chem. Eng. J.* **2025**, 521, 166767.

[S10] Ding, P. L.; Pan, X.; Zhou, X.; et al. Grafting-engineered biomass-based quasi-solid composite electrolyte with suppressed filler aggregation and enhanced interfacial compatibility for high-performance solid-state lithium metal batteries. *Chem Eng J.* **2026**, 530, 173400.

[S11] Mai, W. Q.; Cao, Q. Y.; Zheng, M. T.; et al. A fast ionic transport copolymeric network for stable quasi-solid lithium metal battery. *J Energy Chem.* **2023**, 87, 491-500.

[S12] Hu, Y.; Zhang, W.; Shi, J. P.; et al. Strengthened high-concentration quasi-solid electrolytes for lithium metal with ultralong stable cyclability. *ACS Nano* **2024**, 18 (49)**,** 33418-33429.